Label-free metabolic imaging by mid-infrared optoacoustic microscopy in living cells

Miguel A. Pleitez[1,2]*, Asrar Ali Khan[3,4,5,6], Alice Soldà[1,2], Andriy Chmyrov[1,2], Josefine Reber[1,2], Francesca Gasparin[1,2], Markus R. Seeger[1,2], Benedikt Schätz[1,2], Stephan Herzig[3,4,5,6], Marcel Scheideler[3,4,5,6], and Vasilis Ntziachristos[1,2]*

[1]*Institute of Biological and Medical Imaging, Helmholtz Zentrum München, Neuherberg, Germany.*

[2]*Chair of Biological Imaging (CBI) and Center for Translational Cancer Research (TranslaTUM), Technische Universität München, München, Germany.*

[3]*Institute for Diabetes and Cancer, Helmholtz Zentrum München, Neuherberg, Germany.*

[4]*Joint Heidelberg-IDC Translational Diabetes Program, Heidelberg University Hospital, Heidelberg, Germany*

[5]*Molecular Metabolic Control, Medical Faculty, Technische Universität München, Germany.*

[6]*German Center for Diabetes Research (DZD), Neuherberg, Germany.*

*Email: miguel.pleitez@helmholtz-muenchen.de; v.ntziachristos@helmholtz-muenchen.de

We develop mid-infrared optoacoustic microscopy (MiROM) for label-free bond-selective live-cell metabolic imaging, enabling spatiotemporal monitoring of carbohydrates, lipids, and proteins in cells and tissues. Using acoustic detection of optical absorption, MiROM converts mid-infrared sensing into a positive-contrast imaging modality with negligible photodamage and high sensitivity. We use MiROM to observe changes in intrinsic carbohydrate distribution from a diffusive spatial pattern to tight co-localization with lipid droplets during adipogenesis.

Label-free dynamic imaging of biomolecules in living cells remains challenging for optical microscopy; at wavelengths below 700 nm, it is fundamentally hampered due to lack of chemical specificity or by cellular phototoxicity. Contrarily, chemically specific vibrational imaging modalities such as spontaneous or coherent Raman scattering and mid-infrared (**mid-IR**) microscopy have enormously extended possibilities for endogenous biomolecular imaging[1–3]. Stimulated Raman scattering (**SRS**) microscopy, for instance, can rapidly image tissues at high spatial resolution[4,5]. However, Raman imaging may photodamage cells[6] and its sensitivity is above 1 mM[1], which misses biomolecules in the physiologically relevant micro- to

nanomolar range. Raman imaging of carbohydrates has been demonstrated mainly in fixed cells[7,8], in living cells after using labelling (*i.e.* isotopic labeling) or glucose analogs[5,9], and in densely-packed starch granules in microalgae[10]. Direct vibrational excitation by mid-IR absorption complements Raman imaging[3] (**Supplementary Table 1**). Based on photon absorption, rather than scattering, mid-IR spectroscopy/imaging offers cross-sections up to eight orders of magnitude larger than Raman imaging for certain molecules[3,11,12], sensitively detecting the CH bond and the fingerprint spectral region[3]. Nevertheless, this modality is poorly suited to metabolic studies of living cells because water strongly attenuates mid-IR light and because it applies negative-contrast detection (*i.e.* the stronger the attenuation, the weaker the signal detected). Typically, samples are placed within thin cuvettes (~10-25 μm thick) and irradiated with high-powered mid-IR sources[13,14]. Such confinement perturbs normal cellular behavior and proliferation.

Here we introduce mid-IR optoacoustic microscopy (**MiROM**), a bond-selective imaging modality based on biomolecule-specific vibrational transitions and radiation-less deexcitation for highly efficient optoacoustic generation/detection **(Fig. 1)**. We hypothesized that MiROM could offer label-free detection for all types of biomolecules with high signal-to-noise ratio (**SNR**) and contrast-to-noise ratio (**CNR**). MiROM relies on detection of ultrasound waves, which are attenuated much less than mid-IR photons; ultrasonic detection also renders MiROM as a positive-contrast method; *i.e.* the stronger the attenuation, the stronger the signal detected. The unique combination of positive-contrast sensing and low-attenuation detection-path balances signal loss, allowing deeper imaging than standard mid-IR microscopy. Here MiROM was implemented in trans-illumination, which allowed diffraction-limited optical excitation with confocal ultrasound detection (**Fig. 1a**). A mid-IR absorption-contrast micrograph was obtained by raster-scanning the sample within the focal plane, simultaneously acquiring optoacoustic signal from specific biomolecular vibrations. With the system presented here, using an average laser power of only 330 μW, we obtained a limit of detection (**LOD**) of 2.5 mM for dimethyl sulfoxide (**DMSO**) (**Supplementary Fig. 1a,b**). For comparison, coherent anti-Stokes Raman scattering (**CARS**) has an LOD of 70 mM for DMSO at an average laser

power of ~100 mW[12,15], while SRS detects up to 21 mM of DMSO at similar irradiation power[12,16]. Moreover, we obtained an LOD of 1.5 µM for protein (albumin) in D_2O using only 500 µW laser power (**Supplementary Fig. 1c-g**), which promises live-cell chemical microscopy at significantly lower risk of phototoxicity[6] (**Supplementary Fig. 2**).

First, we demonstrated the full biomolecular-contrast coverage of MiROM *in vitro* in comparison with standard ATR-FTIR spectroscopy (**Fig. 1b,c**; **Supplementary Fig. 3**; **Supplementary Tables 2-5**). Next, we demonstrated its bond-selective live-cell imaging capabilities by mapping the lipid and protein content in HeLa cells, undifferentiated 3T3-L1/PreBAT preadipocytes, and differentiated 3T3-L1 adipocytes. The symmetric CH_2 vibration of lipids (around 2850 cm^{-1}) and the amide II band of proteins (around 1550 cm^{-1}), mainly NH bending and CN stretching, were excited. Imaging wavenumbers were fine-tuned by live-cell optoacoustic spectroscopy (**Fig. 1h,i**). The spatial (lateral) resolution of the system (~5.3 µm at 2850 cm^{-1}, **Supplementary Fig. 4a,b**) resolved single cells and individual lipid droplets (**LD**s) in differentiated 3T3-L1 adipocytes (**Fig. 1d-h**). In HeLa cells and undifferentiated preadipocytes, micrographs at the CH_2 vibration (lipid-map) show the phospholipid membrane (**Supplementary Fig. 5**) at CNRs up to 22:1 (SNRs around 30:1, **Methods**). In differentiated adipocytes, the dominant contrast comes from LDs because they contain more triglycerides than the cell membrane and culture medium (**CM**). CNRs up to 220:1 and SNRs up to 223:1 were observed.

Positive contrast in amide II micrographs (protein-map) originated mainly from the overall protein content, with a weak contribution from water. CNRs up to 41:1 and SNRs around 80:1 (**Supplementary Fig. 6a**). LDs showed negative contrast because they are hydrophobic and contain less protein than the cytoplasm. The absolute contrast of LDs in the protein-map was nevertheless high enough to be detected at SNRs up to 46:1, perhaps because of LD-associated proteins (**Supplementary Fig. 6a**).

Besides lipids and proteins, carbohydrates were also detected in living 3T3-L1 adipocytes after excitation between 1085 and 1000 cm^{-1} (C–O stretching and C–O–H deformation). Localized

contrast was found in the cell body around the growing LDs with CNRs up to 24:1 and SNRs around 40:1 (FOV: 50 µm x 50 µm; imaging time: < 1 min/frame, **Fig. 2a-e**). One possible explanation for the presence of carbohydrates in the cell body might be the capture and accumulation of glucose for biosynthesis of triglycerides to be packed into LDs during lipogenesis. This observation is supported by measurements in differentiating 3T3-L1 cells where the molecular contrast (lipid, protein, and carbohydrate) was monitored in large FOVs (1.5 mm x 1.5 mm) during several days (**Fig. 2f-n**). Glucose uptake was manipulated by changing the concentrations of glucose and insulin in the medium (**Methods**). Carbohydrate contrast increased in cells when incubated in 25 mM glucose and 1 µg/mL insulin (**Fig. 2g-i,n;** days 2, 4, and 6), and it decreased when incubated in 5 mM glucose only (**Fig. 2j,k,n;** days 8 and 10). These changes in MiROM carbohydrate contrast agreed with a standard colorimetric assay of total carbohydrate (**Supplementary Fig. 7**, **Methods**). The carbohydrate contrast was initially diffuse in the cell body and later co-localized with LDs during incubation (**Supplementary Fig. 8**). This may reflect the appearance of glycoproteins or glycolipids in LDs or their membranes.

We used MiROM to monitor lipid and protein dynamics during isoproterenol-induced lipolysis in white adipocytes (differentiated 3T3-L1) and brown adipocytes (differentiated PreBAT) during 4 hours. Lipid-maps (at 2857 cm^{-1}) and protein-maps (at 1550 cm^{-1}) were taken every 5 min before and after addition of isoproterenol to the medium (**Methods**). In both adipocyte types, overall lipid content slowly increased before lipolysis, reflecting ongoing lipogenesis. After induction, lipid contrast decreased continuously and nearly linearly (**Fig. 1m,n; Supplementary Fig. 9a-d**). Different white adipocytes exhibited different lipolysis rates, with some adipocytes unaffected by isoproterenol. Absorption of smaller LDs by larger ones (*i.e.* LD remodeling) was continuously observed in some adipocytes (**Fig. 1m, ROI 1**). Other adipocytes dimmed noticeably after lipolysis induction (**Fig. 1m, ROI 2**). The same heterogeneous response to isoproterenol was observed in brown adipocytes (**Supplementary Fig. 9a,c,d**). As expected, lipolysis was faster and more extensive in brown than in white adipocytes: by 2 hours, lipid contrast had changed up to 30% in brown adipocytes, compared

to 18% in white adipocytes (**Videos 1a,b** and **2a,b**). Similar heterogeneous changes in protein contrast were observed in cells during lipolysis (**Videos 3a,b**; **Supplementary Fig. 9e,f** and **Supplementary Fig. 10**). This may reflect adipokine secretion, protein degradation and/or protein translation. Changes in protein contrast may also reflect conformational changes because amide II is relatively conformation-dependent[17].

To demonstrate the potential of MiROM to image deeper in thicker samples than with standard mid-IR imaging, we applied MiROM in a 4-mm-thick slice of freshly excised pancreatic (mouse) tissue (**Fig. 1j-l**). Lipid micrographs show the pancreatic acinar glands in positive contrast (CNR up to 58:1), while protein micrographs show, in negative contrast, the compartments where acinar glands are embedded (CNR up to 21:1) (**Supplementary Fig. 6b**). Similar or higher CNRs were observed in other similarly thick tissues (**Supplementary Fig. 11** and **Supplementary Fig. 12**). A maximum imaging depth of 90 μm was obtained for the acinar glands (**Supplementary Fig. 13**), compared to 575 μm in fat/polyamide-suture phantoms (**Supplementary Fig. 14**). Regarding imaging speed, MiROM enables imaging FOVs of 5 mm x 5 mm in steps of 10 μm (pixel size) in ~16 min.

MiROM offers unprecedented high contrast, image quality, sensitivity, and specificity for endogenous biomolecular microscopy of living cells and thick unprocessed freshly-excised tissues with negligible photodamage. For the first time, we visualize how carbohydrates initially spread throughout young adipocytes, then co-localize with LDs upon adipocyte maturation. MiROM can monitor intrinsic lipid/protein changes of <1% during lipolysis. MiROM is based on vibrational excitation by mid-IR absorption and positive-contrast detection, so it offers great sensitivity in the fingerprint spectral region, with LODs of 2.5 mM for DMSO and 1.5 μM for albumin at laser powers in the 100's of μW. Most LDs visualized by confocal microscopy were also resolved by MiROM, though the two types of images differed slightly, especially for structures < 5 μm (**Supplementary Fig. 15**). Resolution of MiROM may be improved by pump-and-probe optoacoustic/optothermal signal read-out[11,18,19] or ultra-wide bandwidth ultrasound detectors[20].

Beyond carbohydrates, lipids, and proteins, MiROM can be used to analyze nucleic acids and water in practically any other cell culture or tissue (shown *in vitro* in **Supplementary Fig. 3**). In this way, MiROM supports live-cell metabolic research and analytical histology, while filling an important gap in label-free biomolecular imaging and considerably extending the contrast range of optoacoustic microscopy.

Acknowledgements

The research leading to these results has received funding from the Deutsche Forschungsgemeinschaft (DFG), Germany [Gottfried Wilhelm Leibniz Prize 2013; NT 3/10-1], as well as from the European Research Council (ERC) under the European Union's Horizon 2020 research and innovation programme under grant agreement No 694968 (PREMSOT). The authors thank Dr. A. Georgiadi, IDC/HMGU, for advice, discussion, and support on mouse adipocyte tissue preparation.

Author Contributions

M.A.P. created the imaging concept, designed, built, and characterized the imaging system. **M.A.P.**, **A.A.**, and **J.R.** designed and performed the experiments on adipocytes. **M.A.P.** and **J.R.** designed and performed the experiments on excised tissues. **A.C.** synchronized and automated the imaging system. **M.R.S.** performed the image processing and prepared the art work**. M.A.P.** and **A.S.** designed and performed the molecular contrast validation experiments and viability test on cells. **M.A.P.**, **F.G.**, and **B.S.** designed and performed the spectral validation of the system. **M.A.P.** processed the results, prepared the images, and wrote the manuscript. **M.A.P.**, **A.A.**, **J.R.**, and **M.S.** analyzed the results on lipolysis. **M.S.** and **S.H.** supervised the study on lipolysis. **V.N.** supervised the whole study. All authors edited the Manuscript.

Ethics declarations

Competing Interests

V.N. have financial interests in iThera Medical GmbH, equity owner and consultant; SurgVision BV / Bracco Sp.A, member of the Scientific Advisory Board; Spear UG, owner. These companies, however, did not contribute to this work. **V.N.** and **M.A.P.** are inventors on a provisional patent application related to mid-infrared optoacoustic microscopy.

Bibliography

1. Cheng, J.-X. & Xie, X. S. Vibrational spectroscopic imaging of living systems: An emerging platform for biology and medicine. *Science (80-.).* **350**, aaa8870–aaa8870 (2015).
2. Baker, M. J. *et al.* Using Fourier transform IR spectroscopy to analyze biological materials. *Nat. Protoc.* **9**, 1771–91 (2014).
3. Diem, M. *et al.* Molecular pathology via IR and Raman spectral imaging. *J. Biophotonics* **6**, 855–886 (2013).
4. Prince, R. C., Frontiera, R. R. & Potma, E. O. Stimulated Raman Scattering: From Bulk to Nano. *Chem. Rev.* **117**, 5070–5094 (2017).
5. Li, J. & Cheng, J.-X. Direct Visualization of De novo Lipogenesis in Single Living Cells. *Sci. Rep.* **4**, 6807 (2014).
6. Minamikawa, T. *et al.* Photo-Induced Cell Damage Analysis for Single- and Multifocus Coherent Anti-Stokes Raman Scattering Microscopy. *J. Spectrosc.* **2017**, 1–8 (2017).
7. Yosef, H. K. *et al.* Noninvasive Diagnosis of High-Grade Urothelial Carcinoma in Urine by Raman Spectral Imaging. *Anal. Chem.* **89**, 6893–6899 (2017).
8. Kallepitis, C. *et al.* Quantitative volumetric Raman imaging of three dimensional cell cultures. *Nat. Commun.* **8**, (2017).
9. Hu, F. *et al.* Vibrational Imaging of Glucose Uptake Activity in Live Cells and Tissues by Stimulated Raman Scattering. *Angew. Chemie - Int. Ed.* **54**, 9821–9825 (2015).
10. Chiu, L., Ho, S. H., Shimada, R., Ren, N. Q. & Ozawa, T. Biotechnology for Biofuels Rapid in vivo lipid / carbohydrate quantification of single microalgal cell by Raman

spectral imaging to reveal salinity □ induced starch □ to □ lipid shift. *Biotechnol. Biofuels* 1–9 (2017). doi:10.1186/s13068-016-0691-y

11. Zhang, D. *et al.* Depth-resolved mid-infrared photothermal imaging of living cells and organisms with submicrometer spatial resolution. *Sci. Adv.* **2**, (2016).

12. Zhang, C. & Cheng, J. X. Perspective: Coherent Raman scattering microscopy, the future is bright. *APL Photonics* **3**, 090901 (2018).

13. Haase, K., Kröger-Lui, N., Pucci, A., Schönhals, A. & Petrich, W. Real-time mid-infrared imaging of living microorganisms. *J. Biophotonics* **9**, 61–6 (2016).

14. Martin, M. C. *et al.* 3D spectral imaging with synchrotron Fourier transform infrared spectro-microtomography. *Nat. Methods* **10**, 861–4 (2013).

15. Hong, W. *et al.* In situ Detection of a Single Bacterium in Complex Environment by Hyperspectral CARS Imaging. *ChemistrySelect* **1**, 513–517 (2016).

16. Liao, C.-S. *et al.* Stimulated Raman spectroscopic imaging by microsecond delay-line tuning. *Optica* **3**, 1377 (2016).

17. Oberg, K. A., Ruysschaert, J.-M. & Goormaghtigh, E. The optimization of protein secondary structure determination with infrared and circular dichroism spectra. *Eur. J. Biochem.* **271**, 2937–2948 (2004).

18. Lee, E. S. & Lee, J. Y. High resolution cellular imaging with nonlinear optical infrared microscopy. *Opt. Express* **19**, 1378–1384 (2011).

19. Shi, J. *et al.* High-resolution, high-contrast mid-infrared imaging of fresh biological samples with ultraviolet-localized photoacoustic microscopy. *Nat. Photonics* (2019). doi:10.1038/s41566-019-0441-3

20. Aguirre, J. *et al.* Precision assessment of label-free psoriasis biomarkers with ultra-broadband optoacoustic mesoscopy. *Nat. Biomed. Eng.* **1**, 0068 (2017).

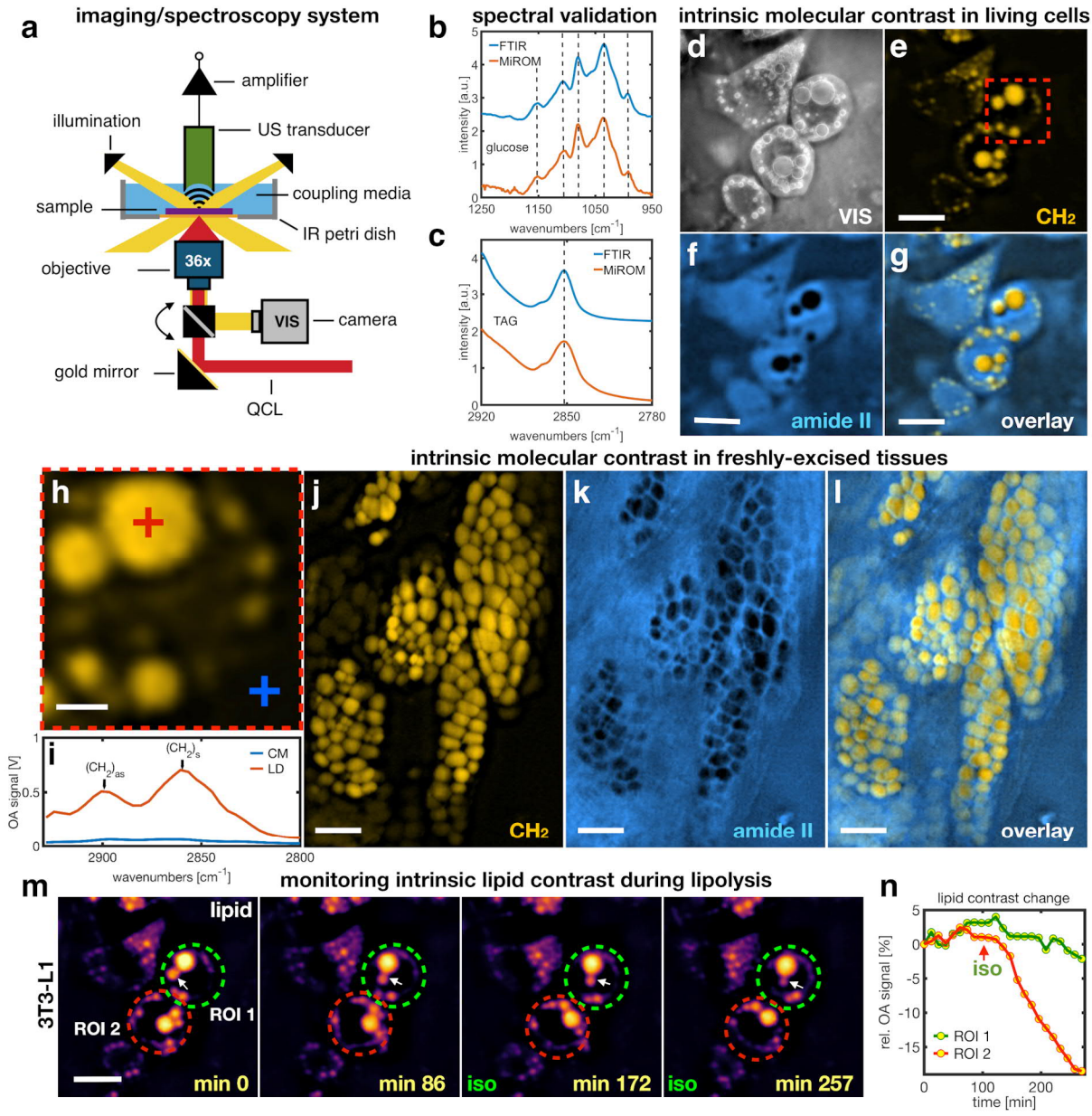

Figure 1: Mid-IR optoacoustic microscopy (MiROM). **a**, Excitation-sample-sensor configuration for MiROM. Focused ultrasound (**US**) transducer and objective are confocally aligned to the sample plane. **b**,**c**, Comparison of MiROM and ATR-FTIR spectrum of glucose and 1,2-dioleoyl-3-palmitoyl-rac-glycerol (**TAG**) *in vitro*. The vertical dashed lines indicate good spectral matching between both methods. **d**, brightfield image of differentiated 3T3-L1 cells. **e-g**, MiROM micrographs of the cells in **d** with endogenous lipid contrast **(e)** at 2857 cm^{-1} (CH_2 vibration) and protein contrast **(f)** at 1550 cm^{-1} (amide II). **g**, Overlay of lipid and protein maps. **h**, Zoom-in on a single adipocyte; dashed red square in **e**, scale bar: 10 µm. Two spots for spectral analysis and fine tuning of the imaging wavelength have been marked; on a lipid

droplet (**LD**) (red cross) and on the cell media (**CM**) (blue cross). **i**, Optoacoustic spectra in the CH vibrational region for the selected spots in **h**. **j-l**, MiROM micrographs of freshly excised pancreatic mouse tissue of 4 mm thickness, scale bar: 100 µm. **j**, Lipid map at 2850 cm^{-1}. **k**, Protein map at 1550 cm^{-1}. **l**, Overlay of lipid and protein maps. Here, clusters of pancreatic acinar glands embedded in protein are observed. **m**,**n**, Monitoring induced lipolysis in differentiated 3T3-L1 adipocytes. **m**, Lipid monitoring sequence at 2857 cm^{-1}. Two region-of-interest (**ROI**) enclosing individual adipocytes are marked, green dashed circle for ROI 1 and red dashed circle for ROI 2. The white arrow follows the process of LD remodeling in a single adipocyte enclosed in ROI 1. Time and presence of ISO is indicated at the bottom corners of each frame (see also **Videos 2a,b**). **n**, Relative lipid contrast change for ROI 1 and 2 in **m**; the red arrow indicates when ISO was added. Scale bar in **e-g**, **m**: 40 µm. Data in **b-n** are representative of five independent experiments.

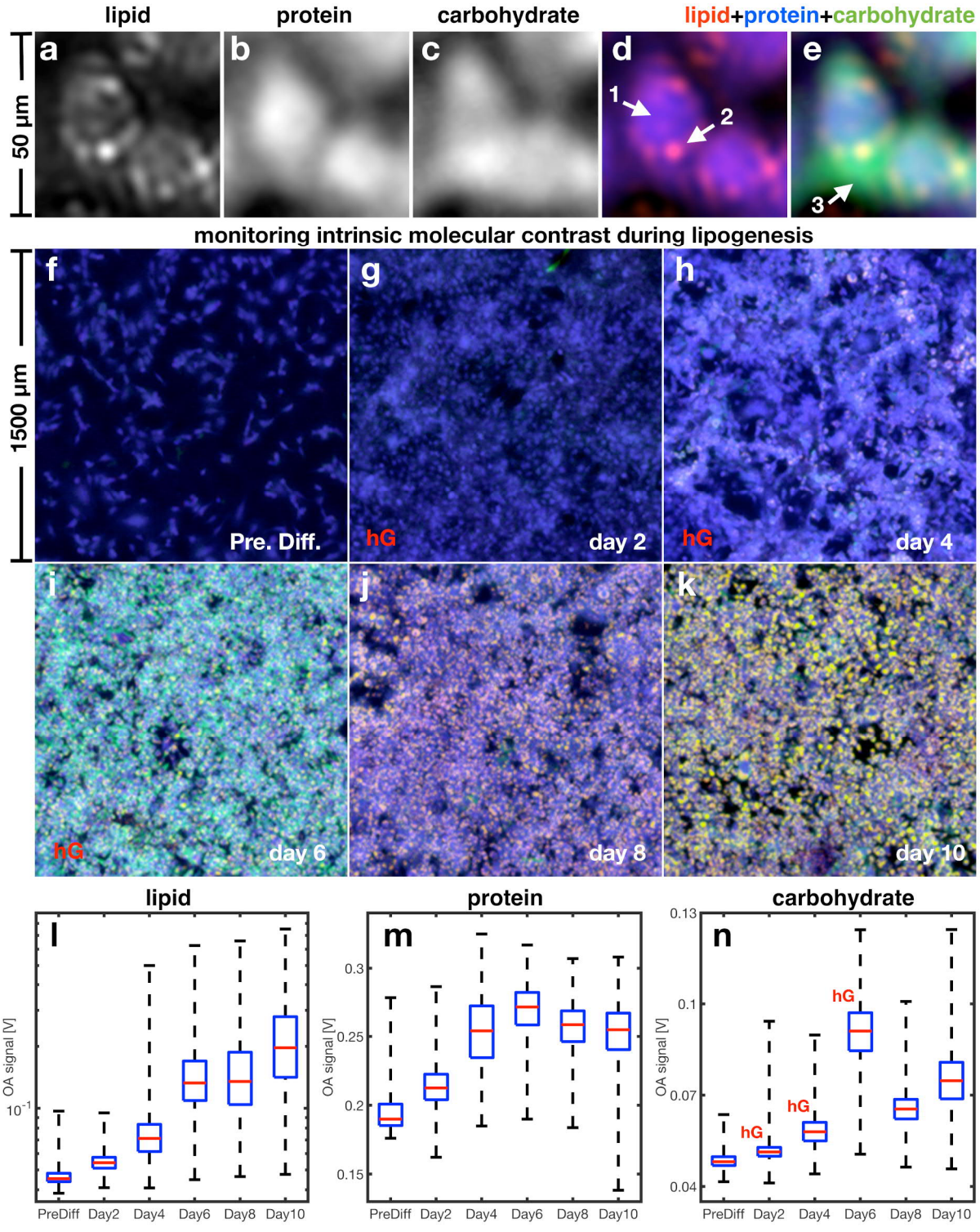

Figure 2: **Monitoring of carbohydrate contrast on 3T3-L1 adipocytes during LD formation**. **a-e**, MiROM micrographs of 3T3-L1 cells at differentiation day 6; imaging speed: < 1 min per channel. **a**, Lipid map at 2853 cm^{-1}. **b**, Protein map, sum of amide I and II. **c**, Carbohydrate map, sum of 1081 cm^{-1} and 1084 cm^{-1}. **d**, Overlay of lipid (red) and protein (blue) maps. **e,** Same picture in **d** adding the carbohydrate (green) map. Arrow 1 indicates proteins

in the cell body, arrow 2 indicates an LD, and arrow 3 indicates an area of carbohydrate accumulation around the growing LDs. **f-k**, Merged lipid (2857 cm^{-1}), protein (1541 cm^{-1}), and carbohydrate (1022 cm^{-1}) maps of 3T3-L1 cells at different incubations days towards LD formation; imaging speed: 16 min per channel. The overall carbohydrate contrast increases after differentiation is started and it is broadly distributed in the cells at day 6 (CNR of 24:1 and SNR of 40:1) around the areas of LD formation as in **e**. At day 8 and 10, however, carbohydrate contrast is found only sparsely but highly co-localized with the LDs, see also **Supplementary Fig. 8**. **i-n**, Box-plots (n=90,000) of OA contrast for each channel in micrographs **f-k**; box plots indicate the upper and lower quartiles (box limits), median (center line), minimum and maximum values (whiskers)**.** During differentiation (day 2, 4, and 6), the cells show a rapid increase of molecular contrast. Once the cell media is changed to normal incubation media (low glucose concentration, no insulin) after day 6, lipid accumulation is observed at a lower rate while proteins reach a rather stable level and the mean carbohydrate contrast drops, correlating with extra cellular glucose and insulin modulation. The label '**hG**' (red font) indicates when the cells were cultured with differentiation media (high glucose concentration + insulin). Images **a-k** are representative of five independent experiments.

Online Methods

System description

A broadly tunable pulsed Quantum Cascade Laser (**QCL**) (MIRcat, Daylight Solutions, CA, USA) is used for optoacoustic generation and biomolecular specificity; the spectral range of the QCL is 3.4–11.0 µm (2941–909 cm^{-1}) with a spectral linewidth ≤1 cm^{-1} (FWHM). The pulse duration of the QCL is set to 20 ns at a repetition rate of 100 kHz then focused into the sample by a 0.5 NA reflective objective (36x, Newport Corporation, CA, USA). The mid-IR absorption-map of the sample is obtained by scanning the sample along the focal plane by motorized stages (Prior Scientific/Physik Instrumente (PI) , Cambridge/Karlsruhe, UK/DE) simultaneously detecting the optoacoustic signal by a 20 or a 25 MHz central frequency focused ultrasound transducer (Imasonic/Sonaxis, Voray sur l'Ognon/Besancon, France). The focused ultrasound transducer and the reflective objective are coaxially aligned to share the same focal plane

where the sample is placed on a custom-made mid-IR transparent stainless-steel or acrylic-glass petri-dish using a ZnSe window (Edmund Optics, Mainz, DE) or a ZnS window (Crystal GmbH, Berlin, DE) as bottom substrate. For the live-cell studies, the cell media served as acoustic coupling between the US transducer and the cells. Deionized water was used as coupling media otherwise.

To remove interference from atmospheric CO_2 and water vapor, the mid-IR beam-path is purged with a constant flow of dry N_2. A Mercury-Cadmium-Tellurium (**MCT**) detector (Daylight Solutions, CA, USA) is used for optical reference and a VIS laser pointer, co-aligned with the QCL beam, serves as aiming beam for easy optical adjustment. For validation, co-registration, and easy ROI selection, oblique VIS illumination (Edmund Optics, Mainz, DE) is used to obtain standard brightfield micrographs with a general purpose monochromatic camera (Edmund Optics, Mainz, DE) (see **Fig. 1a** and **Supplementary Fig. 4a**).

The laser power at selected and relevant wavenumbers for this work was measured by a mid-IR specific power meter (PE9-ES-C, Ophir-Spiricon, Darmstadt, DE) at 500 ns laser pulse duration and 10 kHz repetition rate just before entering the reflective objective. The average laser power at the sample was calculated scaling the measured values to the pulse duration of 20 ns and repetition rate of 100 kHz taking also into account the obscuration (17%) of the reflective objective. These laser excitation powers were used for all measurements reported here; imaging, spectroscopy, and viability test. This is summarized as follows:

Wavenumber (cm^{-1})	Measured average power at 500 ns and 10 kHz (mW)	Equivalent laser power at 20 ns, 100 kHz, and 17% obscuration (mW)
2850	0.8	0.27
1650	1.6	0.53
1550	2	0.66
1085	1.9	0.33

Signal recovery, contrast, and noise.

The raw optoacoustic signals were amplified by 63 dB (MITEQ, NY, USA) filtered with a 50 MHz low pass filter (Mini-Circuits, NY, USA) and then recorded at a sampling rate of 250 MS/s on a 12 bit DAQ card, or at 200 MS/s on a 16 DAQ card, (Gage Applied, Lockport, USA). The intensity of each pixel composing the micrographs shown in this work is the peak-to-peak amplitude value resulting from the average of 50 or 100 optoacoustic transients (A-lines); corresponding to a pixel dwell time of 1 ms or 500 µs, respectively, at the pulse repetition rate of 100 kHz.

The signal-to-noise ratio (***SNR***) is defined here as the ratio between the peak-to-peak amplitude value of the optoacoustic signal ($\boldsymbol{OAS_{PkPk}}$) over the peak-to-peak amplitude value of the noise level ($\boldsymbol{Noise_{PkPk}}$) before the arrival of the optoacoustic signal. For instance, the maximum SNR of the lipid-map for the white adipocytes discussed above is 223:1, corresponding to a relative error of 0.45 %. In terms of absolute values this corresponds to an optoacoustic peak-to-peak amplitude of 702.2 mV and a peak-to-peak amplitude of the noise of 3.1 mV. In the protein-map the maximum SNR is close to 80:1, or 1.3 % relative error. This is calculated from an absolute optoacoustic peak-to-peak amplitude of 247 mV and a noise level of around 3 mV.

$$SNR = OAS_{PkPk}/Noise_{PkPk}$$

The contrast-to-noise ratio (***CNR***) is defined here as the intensity difference between a point in the sample ($\boldsymbol{OA_S}$) and a point in the background ($\boldsymbol{OA_B}$) divided over the peak-to-peak amplitude value of the noise level.

$$CNR = |OA_S - OA_B|/Noise_{PkPk}$$

The mean contras-to-background ratio (mean CBR) described in **Supplementary Fig. 7** is the mean contrast obtained from the image histogram divided over the background intensity (OA_B). As explained below, prior to measurements on cells and tissues, the contrast, resolution, spectral accuracy, sensitivity, and imaging depth of the system was tested in synthetic samples: polyamide sutures and polyethylene microspheres embedded in agar, NIST spectral gold standard, and dimethyl sulfoxide (**DMSO**). (**Supplementary Fig. 1**, **Supplementary Fig. 4b-d**, **Supplementary Fig. 14**, and **Supplementary Table 6**).

Spectral validation

First, the absorption spectrum of a NIST traceable Polystyrene calibration film for IR spectroscopy (Sigma-Aldrich, St. Louis, USA) was measured in transmission mode by MiROM. The position of the absorption peaks obtained by MiROM was compared with the certified values of the NIST gold standard. We obtained a minimum deviation of 0.1 cm^{-1} around 1583 cm^{-1} and a maximum deviation of 2.6 cm^{-1} around 2850 cm^{-1} of the spectrum measured by MiROM regarding the gold standard (see **Supplementary Table 6**).

Second, the ability to identify specifically and precisely different biomolecules was demonstrated comparing the optoacoustic spectra obtained by MiROM with the spectra of the same molecules (the same samples) obtained with a standard ATR-FTIR spectrometer (Bruker Corporation, MA, USA).

Four samples representing each of the fundamental classes of biomolecules (namely: glucose, DNA, triglycerides, and albumin) were prepared and measured with MiROM and ATR-FTIR as follows:

A 50g/L water solution of glucose was prepared dissolving 2.5 g of D-(+)-glucose (Sigma-Aldrich, St. Louis, USA) in 50 mL of distilled water.

A 5% water solution of DNA (Deoxyribonucleic acid sodium salt from *Escherichia coli* strain B, Sigma-Aldrich, St. Louis, USA) was prepared dissolving 1 mg of DNA in 20 µL of distilled water. A 5-µL drop of this solution was placed in a carbon tape ring located on a dish and dried under vacuum. The sample was covered with a plastic film to avoid water dilution.

A 10 mg/mL solution of 1,2-dioleoyl-3-palmitoyl-rac-glycerol (TAG) (Sigma-Aldrich, St. Louis, USA) was prepared dissolving 1 mg in 100 µL of a chloroform/methanol solution (2:1). A 10-µL drop of this solution was placed on the window of a dish and dried under vacuum.

An 80g/L D_2O solution of albumin was prepared dissolving 2.0 g of albumin (Carl Roth) in 25 mL of heavy water. As commonly done in standard FTIR spectroscopy, for albumin, D_2O was used instead of H_2O in order to avoid the strong absorption peak of water around 1650 cm^{-1} (**Supplementary Fig. 3d**), overlapping the amide I band of proteins.

All the measurements were performed on the custom-made mid-IR petri-dish with a ZnSe window using carbon tape (SPI Suppliers, PA, USA) as spectral reference. The optoacoustic spectra were measured with a resolution of 2 cm^{-1} and an averaging time of 100 ms per wavenumber. For comparison, a 5-µL drop of each solution was measured with the ATR-FTIR spectrometer equipped with a diamond ATR crystal. The same resolution of 2 cm^{-1}, as with the MiROM system, was used to record the spectra with the ATR-FTIR spectrometer. For water solutions, water was measured and subtracted from both, the optoacoustic and FTIR spectra. As observed in **Fig. 1b,c**; **Supplementary Fig. 3** and **Supplementary Tables 2-5**, MiROM was able to accurately detect the absorption bands of biomolecules.

Determination of the limit of detection (LOD)

We determined the LOD of MiROM for two reference molecules: DMSO in H_2O and albumin in D_2O. For DMSO, the optoacoustic spectrum at different concentrations (from 664 mM to 0.02 mM) was measured between 1250 and 909 cm^{-1}, averaging time ~100 ms per wavenumber (**Supplementary Fig. 1a**). The area under the absorption band of the S=O vibration at 1010 cm^{-1} was selected for determination of the lowest detectable concentration of DMSO, the optoacoustic signal at 1066 cm^{-1} and 984 cm^{-1} were used for spectral baseline correction and normalization, respectively. The area under the normalized optoacoustic intensity of the S=O vibration (**Supplementary Fig. 1b**) as well as its optoacoustic spectra, show that DMSO can be detected, above the spectral baseline, at a concentration of 2.5 mM with a SNR of 6:1. Here, the baseline, or noise level, is defined by the difference of two measured optoacoustic spectra of water. The maximum average laser power in the spectral range measured is 330 µW at around 1085 cm^{-1}, measured as described above.

For albumin, the optoacoustic spectrum at different concentrations (from 750 µM to 1.5 µM) was measured between 1700 and 1600 cm^{-1} (the amide I band), averaging time ~100 ms per wavenumber (**Supplementary Fig. 1d**). The area under the amide I band was selected for determination of the lowest detectable concentration of albumin, the optoacoustic signal at 1700 cm^{-1} and 1600 cm^{-1} were used for spectral baseline correction and normalization, respectively. The area under the normalized optoacoustic intensity of the amide I band

(**Supplementary Fig. 1e**) as well as its optoacoustic spectra show that albumin can be detected, above the spectral baseline, at a concentration of 1.5 µM with an SNR of 4.5:1. Here, the baseline, or noise level, is defined by the difference of two measured optoacoustic spectra of heavy water. The maximum average laser power in the spectral range measured is 530 µW at around 1650 cm^{-1}, measured as described above.

The SNR for the LOD determination (SNR_{LOD}) is defined here as the area of the normalized optoacoustic absorption band of the analyte ($Area_{NOAS}$; the signal), after buffer subtraction, divided by the area of the baseline ($Area_{BL}$; the noise) (absolute value).

$$SNR_{LOD} = Area_{NOAS}/Area_{BL}$$

Image processing

In order to enhance visibility and compensate for spatial resolution of mid-IR microscopy in the range of subcellular compartments of interest (~ 5 µm), the images were bicubic interpolated to a pixel size of 250 nm and deconvolved with the experimental determined point-spread function (see **Supplementary Fig. 4b**) by a 3- or 5-step iterative Wiener deconvolution. Furthermore, the images were post processed by a 2-pixel Gaussian filtering, outlier removal if necessary, a contrast enhancement to a 0.3% saturation, and a histogram normalization. For resolution analysis and SNR determination, the images were kept unprocessed.

Preparation and measurement of white and brown adipocytes

3T3-L1 mouse white preadipocyte cells were plated in the custom plates and cultured till confluency in growth media consisting of: Dulbecco's Modified Eagle's Medium (DMEM) low glucose (1 g/L) (Life Technologies, Paisley, GBR) supplemented with 10% fetal bovine serum (FBS, Merck, Darmstadt, DE) and 1% pen/strep (Life Technologies, Bleiswijk, NLD). Cells were kept in incubator at 37°C, 5% of CO_2. The process of differentiation lasted for 6 days. On day 0 and day 2, differentiation media consisting in DMEM high glucose (4.5 g/L), 10% FBS, 1% pen/strep, supplemented with 1 µg/mL insulin (Sigma, Steinheim, DE), 0.25 µM dexamethaxone (Sigma, Steinheim, DE), 0.5 mM 3-isobutyl-1-methylxanthine (Sigma, Steinheim, DE) and 1/1000 volume ABP (50 mg/mL L-ascorbate, 1 mM biotin, 17 mM

pantothenate; Sigma, Steinheim, DE) was added to the cells. On day 4, differentiation media supplemented only with insulin and ABP was used. From day 6 and on (after MiROM measurements) the cells were kept in growth media (low glucose, no insulin).

The PreBAT cell line was created and provided by Hoppmann, Perwitz et al. (2010) by immortalizing preadipocytes from the intrascapular BAT of newborn mice using the SV40 Large T antigen. The differentiation process also lasted for 6 days starting with induction on day 0 with DMEM growth media (4.5 g/L glucose; Life Technologies, Paisley, Scotland) containing 20 % FBS (Merck, Darmstadt, DE) and 1 % Pen/Strep (Life Technologies, Bleiswijk, Netherlands) with the addition of 20 nM insulin (Sigma, Steinheim, DE), 1 µM triiodothyronine (T_3) (Sigma, Steinheim, DE), 0.125 mM indomethacin (Sigma, Steinheim, DE), 2 µg/ml dexamethasone (Sigma, Steinheim, DE) and 0.5 mM 3-isobutyl-1-methylxanthine (Sigma, Steinheim, DE). The cells were kept in the incubator at 37°C, 5% of CO_2. On day 2 and day 4, growth media containing only insulin and T_3 was added and on day 6 the cells were given only growth media. At the end of differentiation, both cell lines showed abundant amounts of lipid droplets.

All MiROM measurements on cells where performed using growth media; changing from differentiation media to growth media right before imaging whenever needed.

Quantification of total carbohydrates content

The total amount of carbohydrates in the differentiated 3T3-L1 cell lysates were measured using the Cell Biolabs' Total Carbohydrate Assay Kit (STA-682, Cell Biolabs, San Diego, CA, USA) following the manufacturer's protocol. After each MiROM measurement (at day 0, 2, 4, 6, 8 and 10), the cells were removed from the customized plates upon trypsin digestion and centrifuged at 2000 rpm, for 3 min. The supernatant was discarded and the pellet was washed once with PBS. After centrifugation, the cells were collected and stored at -80 °C. The cells were resuspended at 1-2 x 10^{-6} cell/mL in 1X Assay Buffer. Each pellet was vigorously homogenized and centrifuged to remove the debris. Cell lysates were assayed undiluted in a 96-well plate, 30 µL of each solution was mixed with 150 µL of concentrated sulfuric acid and

incubated for 15 min at 90°C. After addition of a developing solution, containing 5% of phenol in 1X diluent buffer, a chromogen is formed and it can be detected at 490 nm. The samples were analyzed with the microplate reader CLARIOstar (BMG LABTECH) at optical density (OD) 490 nm. For each point, the background OD (acquired before the addition of the developing solution) was subtracted. Experiments were carried out in duplicate.

Cell viability study.

To assess the negligibility of photodamage induced by MiROM, a standard viability test on undifferentiated 3T3-L1 preadipocytes was performed. A 10 µL-drop of cells was plated in a custom-made MiROM dish, with a ZnSe window of 12.7 mm diameter. After overnight incubation in growth media, at 37°C, 5% of CO_2, a FOV of 2 mm x 2 mm was irradiated with a pulse laser of 100 kHz during a total irradiation time of 4 h 40 min: 20 scanning loops (frames) for each excitation wavenumber (1557 and 2850 cm^{-1}), corresponding to 7 min per frame. During the measurement, the cells were kept at 37 °C. Cell viability was assessed using erythrosine B exclusion assay. Cell survival was expressed as the percentage ratio of viable irradiated cells in comparison with the corresponding viable not-irradiated controls. For statistical elaboration OriginPro9.1 Software was used. Reported data corresponded to the mean values ± standard deviation (SD) obtained from three different experiments.

Preparation and measurement of mouse tissues

Male C57BL/6J mice (8-10 weeks old; Charles River Laboratories Inc, Charleston, USA) were kept at 24±1°C and fed with standard rodent diet (Altromin 1314, Altromin Spezialfutter GmbH & Co, Germany) with free access to water, with constant humidity and on a 12-h light–dark cycle. After the mice were sacrificed the organs were harvested and directly placed on the sample holder where they were covered with low temperature melting agar (2%) and de-ionized water as coupling media.

Data Availability Statement

The data that support the findings of this study are available from the corresponding authors upon reasonable request.